Stability analysis of injection molding flows

Stability analysis of injection molding flows

Arjen C. B. Bogaerds, Martien A. Hulsen,

Gerrit W. M. Peters,[a] and Frank P. T. Baaijens

Materials Technology, Department of Mechanical Engineering, Dutch Polymer Institute, Eindhoven University of Technology, P.O. Box 513, 5600 MB Eindhoven, The Netherlands

(Received 15 July 2003; final revision received 9 March 2004)

Synopsis

We numerically investigate the stability problem of the injection molding process. It was indicated by Bulters and Schepens [Bulters and Schepens (2000)] that surface defects of injection molded products may be attributed to a flow instability near the free surface during the filling stage of the mold. We examine the stability of this flow using the extended Pom–Pom constitutive equations. The model allows for controlling the degree of strain hardening of the fluids without affecting the shear behavior considerably. To study the linear stability characteristics of the injection molding process we use a transient finite element algorithm that is able to efficiently handle time dependent viscoelastic flow problems and includes a free surface description to take perturbations of the computational domain into account. It is shown that the fountain flow, which is a model flow for the injection molding process, is subject to a viscoelastic instability. If the various rheologies are compared, we observe that the onset of unstable flow can be delayed by increasing the degree of strain hardening of the fluid (by increasing the number of arms in the Pom–Pom model). The most unstable disturbance which is obtained after exponential growth is a swirling flow near the fountain flow surface which is consistent with the experimental findings. [DOI: 10.1122/1.1753276]

I. INTRODUCTION

We have investigated the stability of a generic fountain flow as depicted in Fig. 1: *right* which is considered as a prototype flow for the injection molding process. During injection molding, flow instabilities can cause nonuniform surface reflectivity. This work is limited to the specific surface defects characterized by shiny and dull bands, roughly perpendicular to the flow direction and alternating on the upper and lower surfaces (Fig. 2). These defects, referred to as flow marks, tiger stripes or ice lines, have been observed in a variety of polymer systems including polypropylene [Bulters and Schepens (2000)], acrylonitrile-styrene-acrylate [Chang (1994)], ethylene-propylene block copolymers [Mathieu *et al.* (2001)] and polycarbonate/acrylonitrile butadiene-styrene (ABS) blends [Hobbs (1996), Hamada and Tsunasawa (1996)]. The occurrence of these defects can limit the use of injection molded parts, especially in unpainted applications such as car bumpers.

From recent experimental findings it is concluded that the surface defects are the result of an unstable flow near the free surface similar to that shown in Fig. 3 [Bulters and

[a]Author to whom correspondence should be addressed; electronic mail: g.w.m.peters@tue.nl

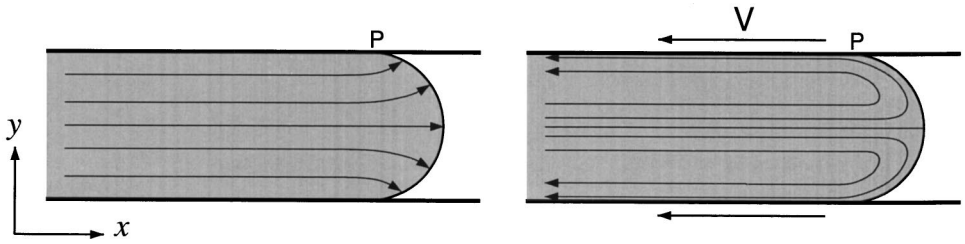

FIG. 1. Kinematics of fountain flow region: Reference frame of mold (*left*) and reference frame of the moving interface (*right*).

Schepens (2000), Chang (1994), Hobbs (1996), Hamada and Tsunasawa (1996), Mathieu *et al.* (2001)]. These experiments also revealed that the cause of the instabilities is of an elastic nature. Due to the limited availability of rheological data, there is no clear understanding of the rheological dependence of the instability, though Chang (1994) found that materials with a higher recoverable shear strain [$S_R = (N_1/2\tau_{xy})$] had less severe flow mark surface defects.

There can be significant difficulties with incorporating elasticity into simulations of the free surface flow because of the geometric singularity which exists at the contact point where the free surface intersects the mold wall as summarized by Shen (1992). Elastic constitutive equations are known to make geometric singularities more severe [Grillet *et al.* (1999), Hinch (1993)]. In order to make elastic injection molding simulations tractable, many researchers have incorporated slip along the wall near the singularity [Sato and Richardson (1995), Mavridis *et al.* (1988)]. Various formulations for the slip condition do not seem to have a strong effect on the kinematics near the free surface, but all formulations seem to ease the difficulties associated with the numerical calculations, especially for elastic constitutive equations [Mavridis *et al.* (1986, 1988), Shen (1992)].

In a previous paper [Bogaerds *et al.* (2003)], a time marching scheme has been developed that is able to handle the complex stability problem of viscoelastic flows with nonsteady computational domains which result from perturbed free surfaces or fluid interfaces. It was shown that this method is able to accurately predict the stability characteristics of a number of single- and multilayer shear flows of upper convected Maxwell (UCM) fluids. Several studies that set out to develop numerical tools that are able to handle complex flow geometries have been troubled by the occurrence of steep boundary layers and poorly resolved continuous spectra [Keiller (1992), Brown *et al.* (1993), Sureshkumar *et al.* (1999), Smith *et al.* (2000)]. From a computational point of view, the UCM model may be suitable for benchmarking of newly developed numerical methods

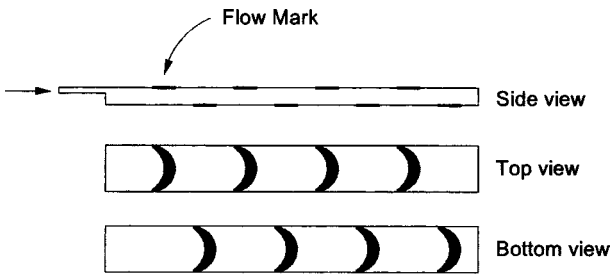

FIG. 2. Characteristic pattern for flow mark surface defects.

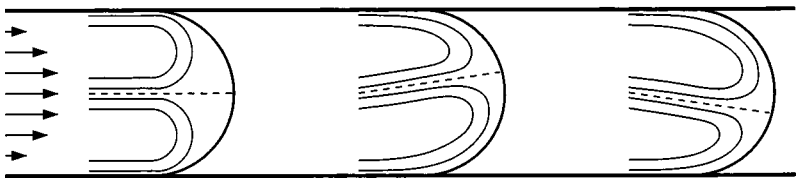

FIG. 3. Unstable flow may cause surface defects.

but it is a rather poor model to study realistic flows of polymer melts as they have material functions that cannot be described by the UCM model. The choice of a constitutive relation is not a trivial one. In Grillet *et al.* (2002a) and Bogaerds *et al.* (2002)], we have shown that generally accepted closed form rheological models like the Phan–Thien–Tanner, the Giesekus and the more recently introduced Pom–Pom model [McLeish and Larson (1998), Verbeeten *et al.* (2001)] show completely different linear stability characteristics in simple shear flows. In order to generate results that are physically meaningful, we need to apply a constitutive set of equations that is able to capture the dynamics of real viscoelastic melts in both shear and elongation. For our computations we use the extended Pom–Pom (XPP) model of Verbeeten *et al.* (2001) because of the ability of the XPP model to accurately describe full sets of viscometric shear and elongational data of a number of polyethylene melts and for limited sets of data of two polypropylenes [Swartjes (2001)].

In the following we first give a short description of the governing set of nonlinear equations that describe the flow. A more extensive treatment of the Pom–Pom and XPP equations can be found in McLeish and Larson (1998) and Verbeeten *et al.* (2001), respectively. The details of the numerical algorithm that is used to study the stability problem are, together with the applied boundary conditions, presented in the appendix. Results of the fountain flow problem are presented in Sec. IV. In an effort to relate material properties to the stability characteristics of the flow, we have studied the behavior of several parameter settings of the XPP model. Also, some of the major problems that trouble the numerical analysis of the fountain flow problem are discussed.

II. GOVERNING EQUATIONS

We assume incompressible, isothermal, and inertia-less flow. In the absence of body forces, these flows can be described by a reduced equation for conservation of momentum (1) and conservation of mass (2):

$$\nabla \cdot \boldsymbol{\sigma} = \mathbf{0}, \tag{1}$$

$$\nabla \cdot \mathbf{u} = 0, \tag{2}$$

with ∇ the gradient operator, and $\mathbf{u}$ the velocity field. The Cauchy stress tensor $\boldsymbol{\sigma}$ can be written as:

$$\boldsymbol{\sigma} = -p\mathbf{I} + \boldsymbol{\tau}, \tag{3}$$

with an isotropic pressure p and the extra stress tensor $\boldsymbol{\tau}$. The set of equations is supplemented with the kinematic conditions that describes the temporal evolution of the free surface

$$\mathbf{n} \cdot \frac{\partial \mathbf{x}}{\partial t} = \mathbf{u} \cdot \mathbf{n}, \tag{4}$$

where **x** denotes the local position vector describing the free surface and **n** is the associated outward normal vector.

In order to obtain a complete set of equations, the extra stress should be related to the kinematics of the flow. The choice of this constitutive relation will have a major impact on the results of the stability analysis [Grillet *et al.* (2002a)]. Motivated by the excellent quantitative agreement of the Pom–Pom constitutive predictions and dynamical experimental data [Inkson *et al.* (1999), Graham *et al.* (2001), Verbeeten *et al.* (2001)], we use the differential form of the XPP model to capture the rheological behavior of the fluid. As is customary for most polymeric fluids, the relaxation spectrum is discretized by a discrete set of M viscoelastic modes

$$\boldsymbol{\tau} = \sum_{i=1}^{M} \boldsymbol{\tau}_i . \tag{5}$$

For a (branched) polymer melt, this multimode approach introduces a set of equivalent Pom–Poms each consisting of a backbone and a number of dangling arms.

Verbeeten *et al.* (2001) have modified the original Pom–Pom model of McLeish and Larson (1998) and effectively combined the set of governing equations into a single relation for the extra stress. Furthermore, they were able to extend the model with a second normal stress difference which is absent in the original Pom–Pom formulation. The XPP model is defined by

$$\overset{\nabla}{\boldsymbol{\tau}} + \left\{ \frac{1}{\lambda_b} \left[\frac{\alpha}{G} \boldsymbol{\tau} \cdot \boldsymbol{\tau} + \mathcal{F}\boldsymbol{\tau} + G(\mathcal{F}-1)\mathbf{I} \right] \right\} - 2G\mathbf{D} = \mathbf{0}, \tag{6}$$

with $\overset{\nabla}{\boldsymbol{\tau}}$ as an auxiliary derivative of the extra stress, $\mathcal{F}$ as an auxiliary scalar valued function

$$\mathcal{F} = 2re^{\nu(\Lambda-1)} \left[1 - \frac{1}{\Lambda} \right] + \frac{1}{\Lambda^2} \left[1 - \frac{\alpha \mathrm{tr}(\boldsymbol{\tau} \cdot \boldsymbol{\tau})}{3G^2} \right], \tag{7}$$

and tube stretch (Λ):

$$\Lambda = \sqrt{1 + \frac{\mathrm{tr}(\boldsymbol{\tau})}{3G}}. \tag{8}$$

The characteristic time scale for relaxation of the backbone orientation is defined by λ_b and relaxation of the tube stretch is controlled by λ_s whereas the ratio of both relaxation times is defined as $r = \lambda_b / \lambda_s$. The parameter ν in Eq. (7) is taken, based on the ideas of Blackwell *et al.* (2000), as $\nu = 2/q$ with q as the number of dangling arms at both ends of the backbone. The plateau modulus is represented by G whereas the kinematics of the flow are governed by fluid velocity **u**, velocity gradient $\mathbf{L} = \boldsymbol{\nabla}\mathbf{u}^T$ and rate of deformation $\mathbf{D} = (\mathbf{L}+\mathbf{L}^T)/2$. The second normal stress difference (N_2) is controlled with the additional parameter α ($N_2 \neq 0$ for $\alpha \neq 0$) which amounts to anisotropic relaxation of the backbone orientation. [Clemeur *et al.* (2003)] showed that for the XPP model and certain parameter sets (nonzero second normal stress difference), turning points can exist for the steady state viscometric functions. In this paper, only parameters sets that result in regular viscometric functions are taken into account (i.e., $\alpha = 0$).] In order to study the influence of the second normal stress difference on the temporal stability of the flow, α can be varied. However, this is beyond the goal of this part of the work and for the remainder of this paper we will assume $N_2 = 0$.

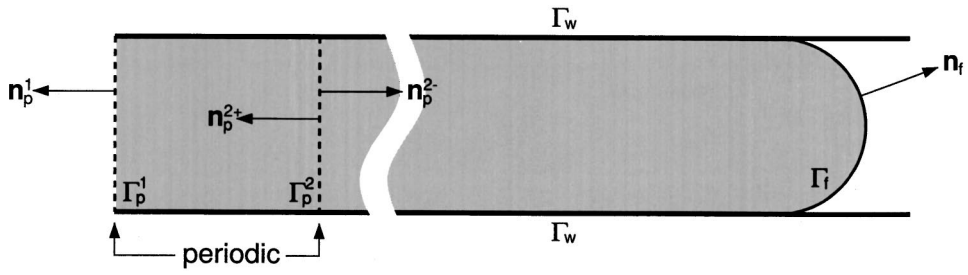

FIG. 4. Computational domain for fountain flow. In addition to the solid walls (Γ_w) there is a free surface (Γ_f) with outward normal $\mathbf{n}_f$. The upstream boundary conditions are imposed on a periodic domain (Γ_p^1, Γ_p^2).

III. NUMERICAL ASPECTS

In this section we discuss the major aspects of the numerical model that is used to determine the linear stability characteristics of the injection molding process. In general, linear stability analysis requires an expansion of the governing equations on the computational domain in which only first order terms of the perturbation variables are retained. Hence, neglecting higher order terms, we may express the physical variables as the sum of the steady state and perturbed values. For instance, we can write for the polymeric stress

$$\boldsymbol{\tau}(\mathbf{x},t) = \tilde{\boldsymbol{\tau}}(\mathbf{x}) + \boldsymbol{\tau}'(\mathbf{x},t), \tag{9}$$

where $\tilde{\boldsymbol{\tau}}$ denotes the steady state value and $\boldsymbol{\tau}'$ denotes the perturbation of the extra stress. Once the steady state values of the unknowns are obtained, the resulting evolution equations for the perturbation variables are solved as a function of time with initially random perturbations of the extra stress variables. The transient calculations are continued until exponential growth (or decay) is obtained for the L_2 norm of the perturbation variables or until the norm of the perturbation has dropped below a threshold value.

The computational domain on which we perform our analysis is presented in Fig. 4. The governing equations for both the steady state and the stability computations are solved using the stabilized DEVSS-**G**/SUPG method [Brooks and Hughes (1982), Guénette and Fortin (1995), Szady *et al.* (1995)]. The spatial discretization based on continuous interpolation for all variables has shown to produce accurate estimates of the stability problem on several occasions using a fully implicit temporal integration scheme [Brown *et al.* (1993), Grillet *et al.* (2002a), Bogaerds *et al.* (2002)]. Here, we employ an operator splitting Θ scheme for the temporal evolution of the perturbed variables.

Due to the presence of a free surface (Γ_f, Fig. 4) during flow, the computational domain does not remain constant during evolution of an arbitrary disturbance. Hence, a temporal integration scheme of the weak formulation of the perturbation equations is used which is able to take linearized deformations of the free surface into account. The issue of the boundary conditions is addressed in Sec. III B. A Newton iteration method is used to obtain two-dimensional steady state results. A description of the finite element steady state analysis and the finite element stability analysis are given in the appendix. Here, we only present the major aspects of the numerical modeling.

A. Finite element stability analysis

Time integration (of the DEVSS-$\bar{\mathbf{G}}$ equations: see appendix) is performed using a second order operator splitting Θ scheme. Application of the operator splitter provides the basis for efficient decoupling of the constitutive equations from the remaining gen-

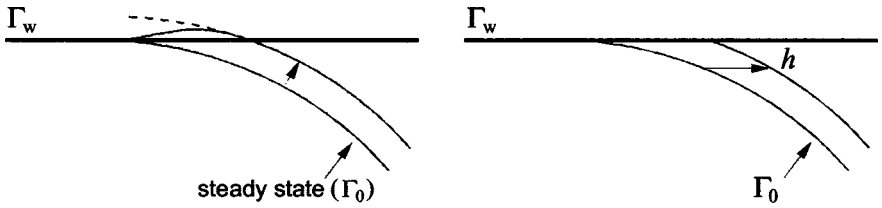

FIG. 5. Computational domain near the contact point of the free surface at the mold wall. Different choices can be made for the surface description. The *left* graph shows the normal displacements whereas the surface description in the *right* graph allows only variations of the wall parallel coordinate.

eralized Stokes equations. Details of the Θ scheme can be found in Glowinski (1991) and Glowinski and Pironneau (1992). The effectiveness of this approach becomes more evident when real viscoelastic melts are modeled for which the spectrum of relaxation times is approximated by a discrete number viscoelastic modes. Based on the work of Carvalho and Scriven (1999), our Θ scheme was developed in Bogaerds *et al.* (2003) together with a domain perturbation technique for the analysis of viscoelastic multilayer flows or free surface flows. It is not necessary to consider deformations of the full computational domain due the fact that only infinitesimal disturbances of the domain in the region of the interface are considered and it suffices to confine the domain perturbations to the interface or free surface. Hence, in addition to the usual perturbed variables (perturbed kinematics and stress), the normal deviation from the steady state interface position was introduced as an auxiliary perturbed variable to describe the deformation of the computational domain.

Following Carvalho and Scriven (1999) and Bogaerds *et al.* (2003), we introduce this new variable h that describes the perturbation of the steady state free surface. However, given the impenetrable solid walls, the deformation of the free surface cannot be consistently described by the normal displacements.

This is easily observed if we consider the flow region near the geometric singularities where the normal displacements should be constrained. On the other hand, without introduction of (numerical) wall slip, the velocity perturbation vanishes in the singularity but there is no reason to assume that this also holds for the surface deformation. Obviously, one of the major difficulties for the fountain flow analysis is to find a consistent formulation for the free surface deformation. Figure 5: *left* shows the problem that arises from the surface description using normal displacements. We could constrain the normal displacement at the singularities as indicated in the figure. However, this would suppress a mode of deformation which may be important for the stability of the flow and, furthermore, we would need to solve a convection dominated problem with the boundary conditions applied to the ''downwind'' nodes. As is shown in Fig. 5: *right*, a consistent alternative formulation is found by taking into account only the wall parallel deformation of the free surface. Other formulations will lead to the generation of nonphysical solutions of the stability problem. A description of the numerical scheme is given in the appendix.

B. Boundary conditions

The analysis is performed in a moving reference frame (Fig. 1: *right*). A consequence of this approach is that the velocity of both confining walls is prescribed which equals the opposite of the frame velocity V. In order to retain a constant amount of fluid within the computational domain, the net flux through the upstream channel should be set to zero. This can be accomplished using different types of boundary conditions. If we consider

the computational domain as depicted in Fig. 4, we may simply prescribe the velocity unknowns on the upstream boundary (Γ_p^1). However, there are two basic reasons to reject this approach. The nonlinear character of the constitutive equations prohibits the use of Dirichlet boundary conditions to obtain true base flow solutions without prior knowledge of the steady state solutions of viscometric channel flows. Furthermore, from an experimental point of view, prescribing local velocity unknowns is very ineffective. Instead, it would be much more convenient to prescribe a global unknown like, for instance, the total flux through the channel which can be measured relatively easy.

An even more important reason not to apply Dirichlet boundary conditions concerns the linear stability analysis. For a fiber drawing flow, it is known that there is a strong dependence of the linear stability on the type of boundary conditions applied, see Pearson (1985), and references therein. Even for this reatively ''simple'' fiber drawing flow it is quite unclear which degrees of freedom should be prescribed. For our generic fountain flow, using a moving frame of reference, we also expect a strong dependence on the boundary conditions if Dirichlet boundary conditions are applied to other boundaries than the two confining walls.

Still, we may regard the upstream region as a planar channel flow. Hence, instead of specifying the necessary upstream degrees of freedom, we consider a part of the upstream flow domain to be periodic on which the volumetric flow rate is prescribed. The major advantage of this approach is that the stability of planar channel flows can be determined separately. In Bogaerds *et al.* (2002), the stability characteristics of planar channel flows of the XPP model using both one-dimensional eigenvalue analyses across the channel gap as well as periodic finite element analyses have been computed. The disadvantage of this approach lies in the fact that an internal periodic boundary condition increases the complexity of the governing equations for both steady state computations and stability analyses. We will enforce the volumetric flow rate by prescribing the velocity of the reference frame at the mold walls and simply assume $Q = 0$ for both the steady state and stability calculations. This is discussed in more detail in the appendix.

IV. RESULTS

The stability of the fountain flow problem is examined using the XPP model. As was already discussed in Sec. II, $\alpha \neq 0$ falls outside the scope of this paper, and hence, we assume $N_2 = 0$ for simple shear flows. The structure of the equivalent Pom–Pom is then fully determined by the nonlinear parameter r (= ratio of relaxation times) and q (= number of arms). The stability of the flow is studied as a function of the relative elastic flow strength, i.e., the dimensionless Weissenberg number We which is defined as

$$\mathrm{We} = \frac{2\lambda_b Q}{H^2}, \tag{10}$$

and is based on the imposed volumetric flow rate Q and a characteristic length scale (half the channel width $H/2$).

It is well known that most rheological models based on tube theory can show excessive shear thinning behavior in simple shear flows. This holds for the original Pom–Pom equations for which the steady state shear stress decreases with increasing shear rate when $\lambda_b \dot{\gamma} = \mathcal{O}(1)$. However, it also holds for certain combinations of the nonlinear parameters of the XPP model although, compared with the original Pom–Pom equations, this maximum is shifted several orders to the right depending on the material parameters.

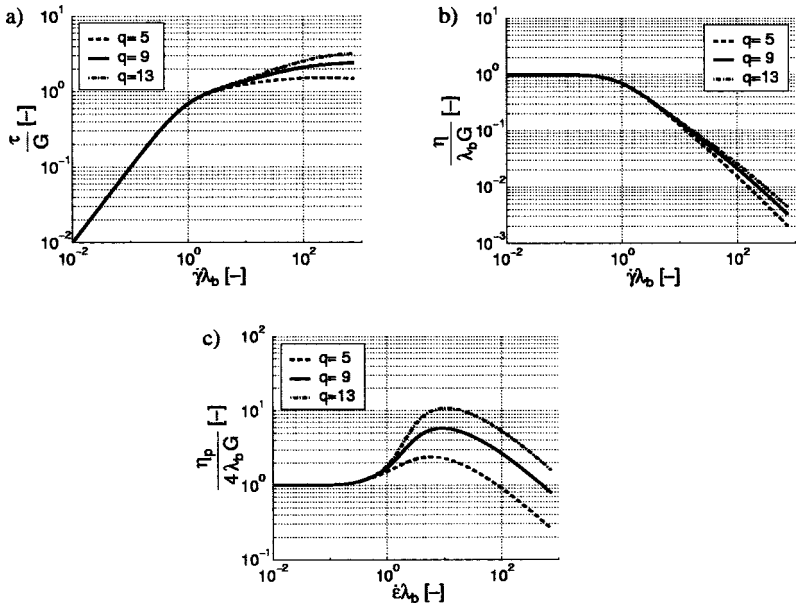

FIG. 6. Steady state viscometric functions (a) shear stress-shear rate, (b) viscosity-shear rate, and (c) planar elongational viscosity-extension rate, for different numbers of arms q and $r = 2$.

We use a single mode model to investigate the influence of the rheology of the polymer melt on the stability behavior of the injection molding process. Therefore, the nonlinear parameters should be chosen in such a way that the shear stress remains a monotonically growing function for the shear rates that fall within the range of the investigated flow situations. In this work we will model differences in polymer melt rheology by variations of the parameter q. Figure 6 shows some of the steady state viscometric functions for different values of the number of arms attached to the backbone ($q = 5,9,13$) and constant ratio of relaxation times ($r = 2$). This choice of parameters has a major impact on the extensional behavior of the model where extensional hardening is increased significantly with increasing number of arms. The influence of the viscometric functions in simple shear is much less severe, although it can be seen that the maximum in the shear stress-shear rate curve shifts to the left when the number of arms is decreased.

A. Steady state results

In this section we present computational results of the viscoelastic fountain flows of the previously described XPP fluids. Table I gives the characteristics of the meshes that were used to analyze both the steady state results as well as the linear stability charac-

TABLE I. Characteristics of the grids used for the fountain flow computations.

	Mesh 1	Mesh 2	Mesh 3
No. of elements	892	1468	2202
No. of elements on free surface	20	30	40
Total length to wetting point		14H	
Length periodic inflow		3.5H	

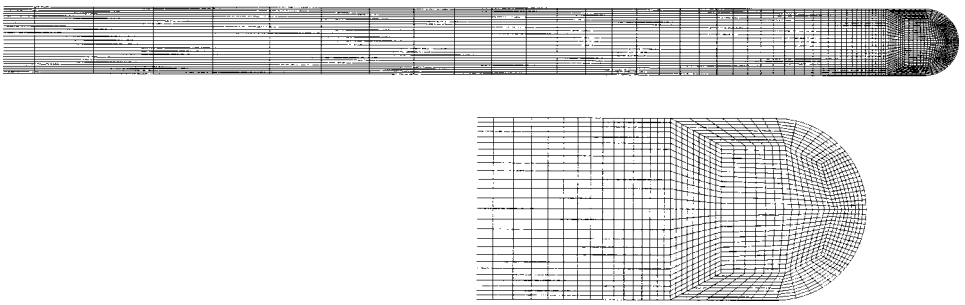

FIG. 7. Finest mesh used for the computations (mesh 3), full mesh and detail of the fountain flow region.

teristics. In the remainder of this section steady state results are presented that are computed on the most refined mesh (mesh 3) which is shown in Fig. 7.

Starting with an initially circular shape of the free surface and using the technique described in the Appendix Sec. A to compute the steady state of the free surface, Fig. 8 shows the base flow solution of the fountain flow surface for various rheologies and Weissenberg numbers. In the left graph, one half of the free surface is shown for $(r,q) = (2,9)$. Comparing the shape of the free surface as a function of We, it can be observed that for small Weissenberg numbers as well as for higher We the shape of the surface is flattened. Moreover, the relative position of the stagnation point on the free surface exhibits a maximum for varying We [Fig. 8 (*right*)]. Due to the differences in the rheologies of the XPP fluids, this maximum shifts considerably to the left for the extensional hardening fluid.

Figure 9 shows some base state variables along the steady free surface. Since the fountain flow surface varies in shape and has therefore variable length, we have scaled the position on the surface by its total length. The left graph shows the tangential velocity along the surface. We observe that in the stagnation point where the fluid deformation is purely extensional, the extension rate is somewhat higher for the strain hardening material. Also, from the right graph, a strong build up of the tangential stress (τ_{tt}) is seen near the walls of the mold whereas the tangential stress is relatively constant for a large part of the free surface. Contour plots for the different rheologies at We = 2.5 are presented in Figs. 10–12. Although there are only minor differences between these graphs, we

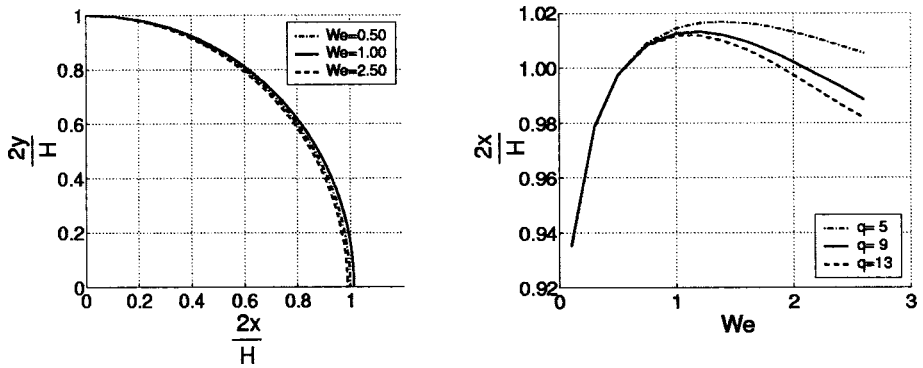

FIG. 8. Shape of the steady state free surface (*left*) for $(r,q) = (2,9)$ and various values of the Weissenberg number. The position of the stagnation point is located at $y = 0$. Position of the stagnation point relative to the intersection with the wall as a function of Weissenberg number (*right*).

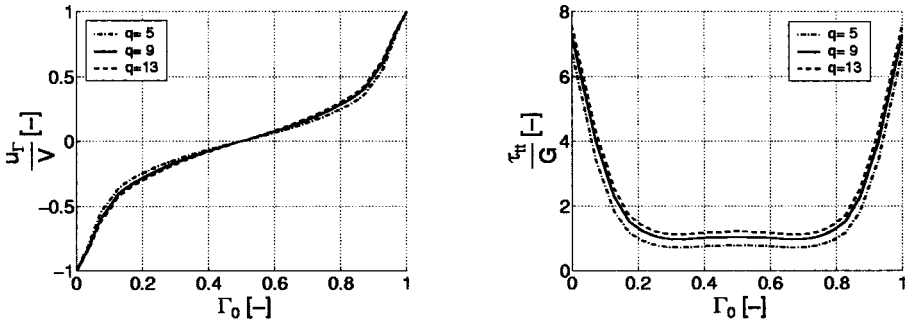

FIG. 9. Steady state velocity (*left*) and the tangential stress τ_{tt} (*right*) on the free surface for We = 2.5 and various values of the number of arms q. The position on the free surface is scaled with the total surface length.

observe that the viscoelastic stress decay more rapidly for $q = 5$. Due to the increasing shear thinning behavior of the fluid with $q = 5$, the streamlines are somewhat more compressed as compared to the more extensional hardening rheologies.

B. Stability results

Results of the linear stability analysis of the fountain flows are presented in this section. Starting with an initially random perturbation of the extra stress tensor, we track the L_2 norm of the perturbed variables in time. Assuming that the most important eigen-

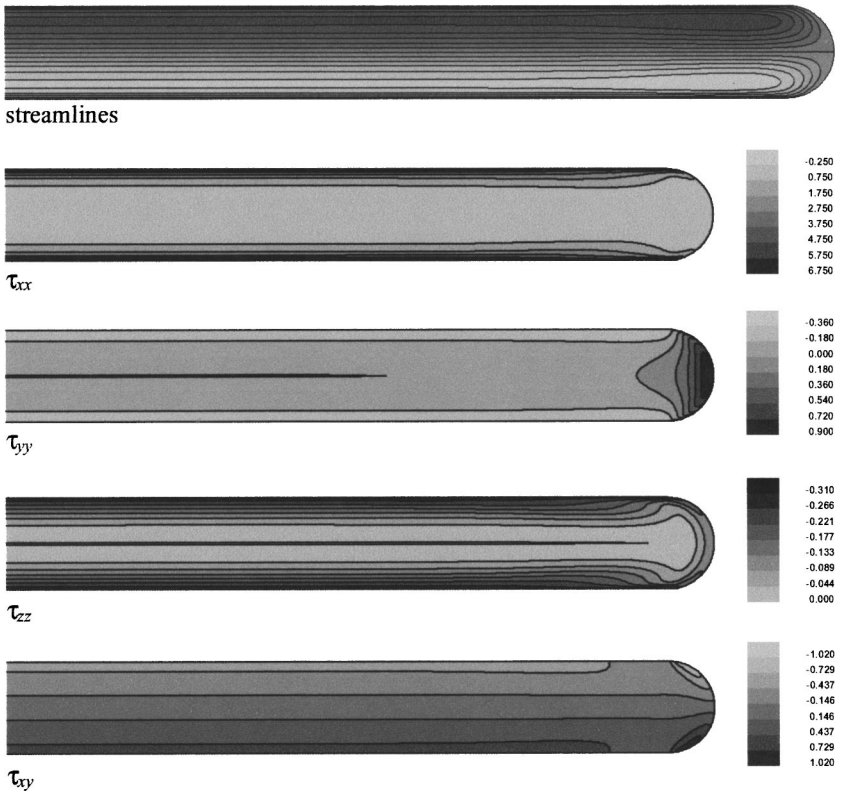

FIG. 10. Steady state result of the XPP fluid for We = 2.5 and $(r,q) = (2,5)$.

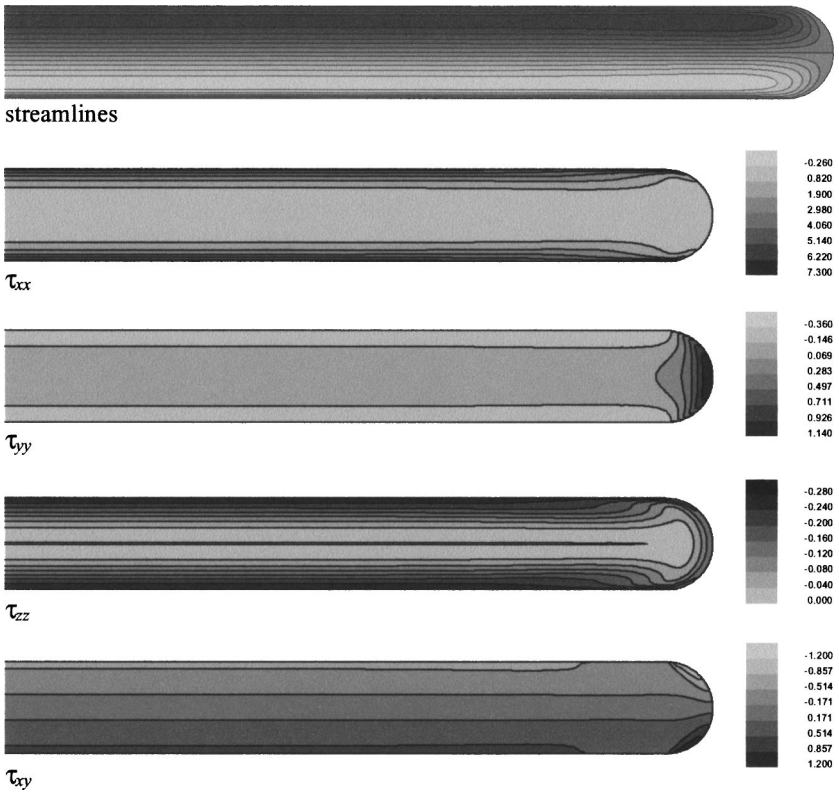

FIG. 11. Steady state result of the XPP fluid for We = 2.5 and $(r,q) = (2,9)$.

modes are excited in this way, exponential behavior will be obtained when all rapidly decaying modes have died out. Hence, the norm of the perturbed variables can grow exponentially in time, in which case we will call the flow unstable, or the norm can decay and the flow will remain stable for the limit of small perturbations. From the temporal growth (or decay) of the perturbation norm, the approximate leading growth rate of the flow is determined which will be larger than zero when the flow is unstable.

In addition to an estimate of the most dangerous growth rate, information is obtained about the structure of the leading eigenmode from the solution of the perturbed variables after exponential growth.

Figure 13 shows the estimated growth rates $(\hat{\sigma})$ for the fountain flow simulations. For the meshes described in Table I and $(r,q) = (2,9)$ stability results are given in the left graph. We observe that the results converge with decreasing grid size. It should be noted though that for all three meshes the grids are relatively coarse in the vicinity of the geometrical singularity. This proved necessary due to the fact that the stability equation for the perturbation of the free surface is very sensitive to disturbances of the wall normal velocity close to the wall when $\partial\tilde{h}/\partial y \rightarrow \infty$ [Eqs. (A17) and (A25)]. Still, the estimated growth rates converges towards a single curve. In the remainder of this paper we will present results that are computed on mesh 3 (Table I).

For the XPP fluid with $(r,q) = (2,9)$ which corresponds to the moderate strain hardening material, we observe that the flow loses stability at We ≈ 2.8.

Similar trends of the stability curves are plotted in the right graph for the other fluids with $(r,q) = (2,5)$ and $(r,q) = (2,13)$. From this figure it is clear that the point of

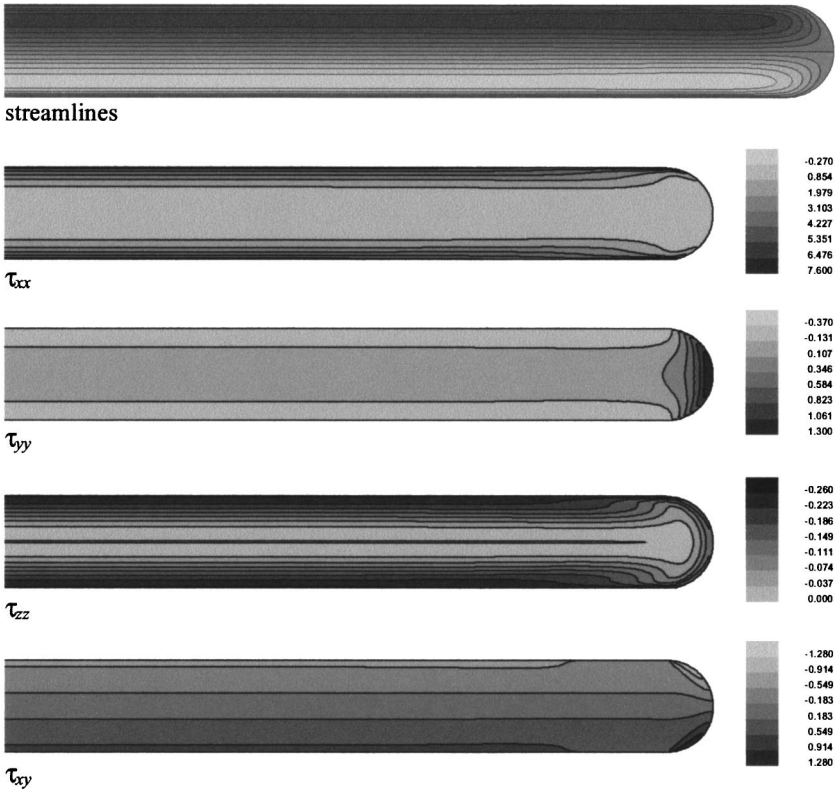

FIG. 12. Steady state result of the XPP fluid for We = 2.5 and $(r,q) = (2,13)$.

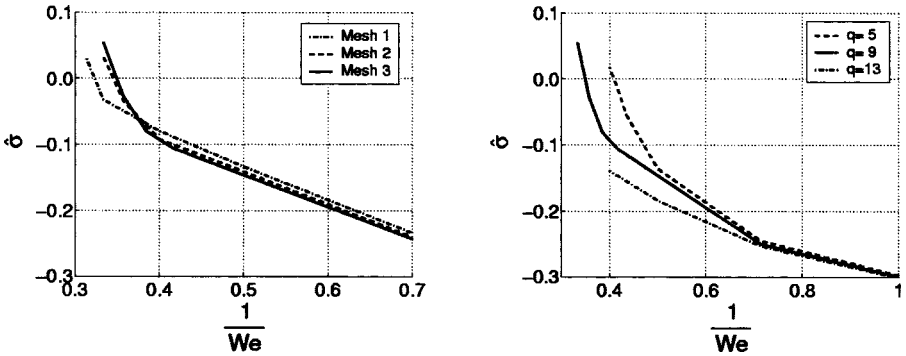

FIG. 13. Comparison of the estimated growth rates for the meshes described in Table I and $(r,q) = (2,9)$ as a function of the inverse Weissenberg number (*left*) as well as linear stability results for several fluid rheologies on mesh 3 and $r = 2$ (*right*).

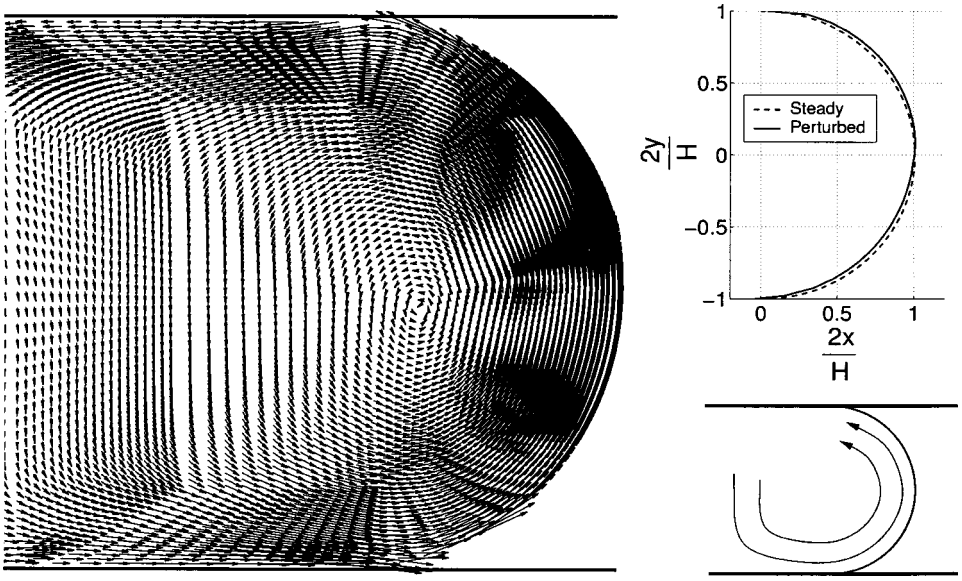

FIG. 14. Results of the linear stability analysis for an XPP fluid for $(r,q) = (2,5)$ and We = 2.5. Shown are the perturbation velocity near the free surface (*left*). Also shown are the linearly perturbed shape of the free surface and a schematic drawing of the swirling flow (*right*).

instability is shifted toward lower Weissenberg numbers when $q = 5$. Although the steady state computations failed to converge for We > 2.5 and $q = 13$, the estimated growth rates are considerably below the other curves which suggests that the flows may be stabilized when q is increased.

After exponential growth or decay, the characteristic eigenfunction of the flow is obtained. For the unstable flow $(r,q) = (2,5)$ at We = 2.5 the perturbation velocity vectors are shown in Fig. 14. It can be seen that this eigenfunction corresponds to a swirling motion very similar to the unstable flows that were observed by Bulters and Schepens (2000). The periodic motion that may be expected from these experiments was not observed during the temporal integration of the disturbance variables. Instead, the perturbation is either clockwise or counter clockwise depending on the initial conditions. If the shape of the perturbed free surface is inspected by adding to the base flow free surface, an arbitrary constant times the surface perturbation h, we obtain the upper right graph of Fig. 14. Summarizing the other flow situations (both stable and unstable), the observed characteristic spatial eigenmode was always similar to the swirling flow near the fountain flow surface.

V. CONCLUSIONS

We have investigated the linear stability of a model injection molding flow by means of a transient finite element algorithm. This work is an extension of earlier work [Grillet *et al.* (2002b)] in which we investigated a similar flow on a fixed computational domain using the Phan–Thien–Tanner model. It is shown that allowing the computational domain to deform due to perturbations of the flow field is an essential feature for the modeling of this viscoelastic instability.

The main goal of this work was to investigate the influence of the fluid rheology on the stability characteristics of the injection molding flows. It was found that a linear

instability sets in at We $\approx$ 2.8 for $(r,q) = (2,9)$. Also, the occurrence of an instability can be postponed when the number of arms in the extended Pom–Pom model is increased. Although this has some effect on the shear properties of the different XPP fluids, the major influence of varying the number of arms can be found in the extensional behavior of the fluids. This would indicate that the flows might be stabilized by fluids with increased strain hardening.

The structure of the leading eigenmode turns out to be a swirling flow near the fountain flow surface. This seems to be consistent with the experimental observations of Bulters and Schepens (2000).

Some care should be taken into account with regard to the singularities where the free surface intersects with both mold walls. From an experimental point of view, the work of Bulters and Schepens (2000) does not show special behavior of the flow around these singularities. However, they do impose a number of numerical difficulties. In this work, all the spatial meshes that have been used are rather coarse near the singularities and although this seems to be justified by the experiments, further investigation of the influence of these points on the overall stability might be necessary.

ACKNOWLEDGMENTS

The authors would like to the acknowledge the support of the Dutch Polymer Institute (DPI), Project No. 129.

APPENDIX

A. Finite element steady state analysis

Using the DEVSS-$\bar{\mathbf{G}}$/SUPG equations, the original three field formulation $(\mathbf{u},\boldsymbol{\tau},p)$ is transformed into a four field formulation $(\mathbf{u},\boldsymbol{\tau},p,\mathbf{G})$ by considering the velocity gradient as an additional dependent variable. If the finite element approximation spaces for $(\mathbf{u},\boldsymbol{\tau},p,\bar{\mathbf{G}})$ are defined by $(\mathcal{U}^h,\mathcal{T}^h,\mathcal{P}^h,\mathcal{G}^h)$, the full set of nonlinear DEVSS-$\bar{\mathbf{G}}$ equations are defined as:

Problem DEVSS-$\bar{\mathbf{G}}$/SUPG: Find $\mathbf{u}\in\mathcal{U}^h$, $\boldsymbol{\tau}\in\mathcal{T}^h$, $p\in\mathcal{P}^h$, and $\bar{\mathbf{G}}\in\mathcal{G}^h$ such that for all admissible test functions $\boldsymbol{\Phi}_u\in\mathcal{U}^h$, $\boldsymbol{\Phi}_{\boldsymbol{\tau}}\in\mathcal{T}^h$, $\Phi_p\in\mathcal{P}^h$, and $\Phi_{\dot{\gamma}}\in\mathcal{G}^h$:

$$\left\{\boldsymbol{\Phi}_{\boldsymbol{\tau}}+\frac{h^e}{|\mathbf{u}|}\mathbf{u}\cdot\boldsymbol{\nabla}\boldsymbol{\Phi}_{\boldsymbol{\tau}},\ \mathbf{u}\cdot\nabla\boldsymbol{\tau}-\bar{\mathbf{G}}\cdot\boldsymbol{\tau}-\boldsymbol{\tau}\cdot\bar{\mathbf{G}}^T+\frac{1}{\lambda_b}\left[\frac{\alpha}{G}\boldsymbol{\tau}\cdot\boldsymbol{\tau}+\mathcal{F}\boldsymbol{\tau}+G(\mathcal{F}-1)\mathbf{I}\right]-G(\bar{\mathbf{G}}+\bar{\mathbf{G}}^T)\right\} = 0, \tag{A1}$$

$$[\boldsymbol{\nabla}\boldsymbol{\Phi}_u^T,\boldsymbol{\tau}+\beta(\boldsymbol{\nabla}\mathbf{u}-\bar{\mathbf{G}}^T)]-(\boldsymbol{\nabla}\cdot\boldsymbol{\Phi}_u,p) = 0, \tag{A2}$$

$$(\Phi_p,\boldsymbol{\nabla}\cdot\mathbf{u}) = 0, \tag{A3}$$

$$(\boldsymbol{\Phi}_{\dot{\gamma}},\bar{\mathbf{G}}^T-\boldsymbol{\nabla}\mathbf{u}) = 0, \tag{A4}$$

with β taken as $\beta = \lambda_b G$ and $(\cdot,\cdot)$ the usual L_2-inner product on the domain Ω. With h^e some characteristic grid size, additional stabilization is obtained by inclusion of SUPG weighting of the constitutive equation [Brooks and Hughes (1982)]. A Newton iteration method is used to obtain two-dimensional steady state results.

The shape of the steady state free surface is solved decoupled from the weak formulation described by Eqs. (A1)–(A4). Each iteration therefore consists of a Newton iteration of Eqs. (A1)–(A4) on a fixed domain (say Ω^{n-1}) after which the position of the nodal points in the computational domain are updated following a new approximation of

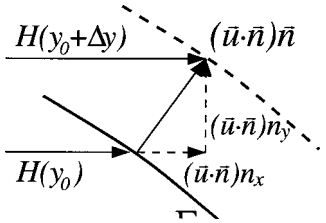

FIG. 15. The x position of the free surface $[H(y)]$ is determined from the local normal velocity $\mathbf{u}\cdot\mathbf{n}$.

the free surface (Γ_f). In order to find this new estimate of the free surface, only variations of the x position of the nodal points on the fountain flow surface are considered. Since the computations are performed in a moving reference frame, the steady state position of the wetting point (wetting line in three dimensions) remains fixed with respect to the frame velocity (V, Fig. 1).

The nth iteration of the free surface shape is obtained in the following way. If the local x position of the free surface of the nth iteration is denoted by $H^n(y)$ (Fig. 15), the steady state formulation of the kinematic condition [Eq. (4)] can be expressed as

$$u_y^n \frac{\partial H^n}{\partial y} - u_x^n = 0, \tag{A5}$$

where $\mathbf{u}^n$ denotes the new velocity approximation on the previous domain (Ω^{n-1}). Since the wetting point is fixed, Dirichlet boundary conditions ($H = constant$) are applied on both mold walls. Obviously, this formulation provides the desired shape of the free surface except for the stagnation point region where H is undetermined since there, both velocity components vanish. On the other hand, it can be seen that near both geometrical singularities, $\partial H/\partial y$ approaches $\pm\infty$ since only u_y vanishes.

In order to resolve the problem associated with the approximate surface near the stagnation point, we define an auxiliary equation for H^n. If the new approximate surface position is found by a displacement in the surface normal direction (Fig. 15) then

$$H^n(y_0+\Delta y) = H^{n-1}(y_0) + [\epsilon(\mathbf{u}^n\cdot\mathbf{n}^{n-1})n_x^{n-1}]_{y_0}, \tag{A6}$$

where n_x denotes the x component of the normal vector and $\Delta y = \epsilon(\mathbf{u}^n\cdot\mathbf{n}^{n-1})n_y^{n-1}$. In general $\mathbf{u}\cdot\mathbf{n}$ will be small and ϵ denotes an $\mathcal{O}(H/V)$ parameter with H as a characteristic length scale. In addition, the first order Taylor expansion for $H(y)$ near y_0 is considered

$$H^n(y_0+\Delta y) = H^n(y_0) + \left(\frac{\partial H^n}{\partial y}\right)_{y_0} \Delta y, \tag{A7}$$

which can be combined with Eq. (A6) to yield the expression

$$H^n + \frac{\partial H^n}{\partial y}\epsilon(\mathbf{u}^n\cdot\mathbf{n}^{n-1})n_y^{n-1} = H^{n-1} + \epsilon(\mathbf{u}^n\cdot\mathbf{n}^{n-1})n_x^{n-1}. \tag{A8}$$

Of course, this expression is not consistent as y approaches the mold walls but, unlike Eq. (A5), it does provide an efficient way to update the free surface near the stagnation point.

The complete set of equations that describes the shape of the free surface is defined using both Eq. (A5) and the inconsistent Eq. (A8). A common approach to obtain a

solution for this overdetermined system is a so called general least squares minimization algorithm [Bochev and Gunzburger (1998)]. It is easily observed that combining Eqs. (A5) and (A8) leads to the desired shape of the interface despite of the fact that Eq. (A8) loses validity near the mold walls. This can be seen since the iterative process is aborted when the L_2 norm of the iterative change of the interface position has dropped below some small value ($\|H^n - H^{n-1}\|_{\Gamma_f} < 10^{-9}$) and Eq. (A8) only converges when $\|\mathbf{u}\cdot\mathbf{n}\|_{\Gamma_f}$ approaches 0:

$$\|H^n - H^{n-1}\|_{\Gamma_f} = \epsilon \left\| (\mathbf{u}\cdot\mathbf{n}) \left[n_x - \frac{\partial H}{\partial y} n_y \right] \right\|_{\Gamma_f} = \epsilon \left\| \frac{\mathbf{u}\cdot\mathbf{n}}{n_x} \right\|_{\Gamma_f} < 10^{-9}, \tag{A9}$$

since $\partial H(y)/\partial y = -n_y/n_x$.

The global iterative process is also aborted when both the L_2 norms of the iterative change as well as the residual of the governing equations have dropped below 10^{-9}.

B. Finite element stability analysis

A short description of the numerical scheme is given; more details can be found in Bogaerds *et al.* (2003). The Θ method allows decoupling of the viscoelastic operator into parts that are ''simpler'' which can be solved more easily than the implicit problem. Hence, if we write the governing linearized equations as

$$\frac{\partial x}{\partial t} = \mathcal{A}(x) = \mathcal{A}_1(x) + \mathcal{A}_2(x), \tag{A10}$$

with x the perturbation variables, the Θ scheme is defined following Glowinski and Pironneau (1992):

$$\frac{x^{n+\Theta} - x^n}{\Theta \Delta t} = \mathcal{A}_1(x^{n+\Theta}) + \mathcal{A}_2(x^n), \tag{A11}$$

$$\frac{x^{n+1-\Theta} - x^{n+\Theta}}{(1-2\Theta)\Delta t} = \mathcal{A}_1(x^{n+\Theta}) + \mathcal{A}_2(x^{n+1-\Theta}), \tag{A12}$$

$$\frac{x^{n+1} - x^{n+1-\Theta}}{\Theta \Delta t} = \mathcal{A}_1(x^{n+1}) + \mathcal{A}_2(x^{n+1-\Theta}), \tag{A13}$$

with time step Δt and $\Theta = 1 - 1/\sqrt{2}$ in order to retain second order accuracy. Formally, only the constitutive equation and the perturbation equation for the free surface contain the temporal derivatives which implies that the left-hand side of Eq. (A10) should be multiplied by a diagonal operator with the only nonzero entrees being the ones corresponding to these equations. The remaining problem is the one that defines the separate operators $\mathcal{A}_1$ and $\mathcal{A}_2$. In essence, we like to choose $\mathcal{A}_1$ and $\mathcal{A}_2$ in such a way that solving Eqs. (A11)–(A13) requires far less computational effort as compared to solving the implicit problem. It is convenient to define $\mathcal{A}_2$ as the advection problem for the extra stress and $\mathcal{A}_1$ as the viscous generalized Stokes problem. With these definitions for $\mathcal{A}_1$ and $\mathcal{A}_2$ and following Bogaerds *et al.* (2003), the weak formulation of our numerical scheme reads:

Problem Θ-FEM step 1[a]: Given the base flow $(\tilde{\mathbf{u}}, \tilde{\boldsymbol{\tau}}, \tilde{\bar{\mathbf{G}}})$ on Ω_0, $\hat{\boldsymbol{\tau}} = \boldsymbol{\pi}(t^n)$ and $\hat{h} = h(t^n)$, find $\mathbf{u} \in \mathcal{U}^h$, $p \in \mathcal{P}^h$, $\bar{\mathbf{G}} \in \mathcal{G}^h$, and $h \in \mathcal{H}^l$ at $t = t^{n+\Theta}$ such that for all admissible test functions $\boldsymbol{\Phi}_u \in \mathcal{U}^h$, $\Phi_p \in \mathcal{P}^h$, $\boldsymbol{\Phi}_{\dot{\gamma}} \in \mathcal{G}^h$, and $\Phi_h \in \mathcal{H}^l$:

$$\left\{\nabla\boldsymbol{\Phi}_u^T,\mathbf{P}^{-1}\cdot\left[\frac{1}{\Theta\Delta t}\hat{\boldsymbol{\tau}}-\mathbf{F}_1(\mathbf{u},\bar{\mathbf{G}})-\mathbf{F}_2(\hat{\boldsymbol{\tau}})\right]+\beta(\nabla\mathbf{u}-\bar{\mathbf{G}}^T)\right\}-(\nabla\cdot\boldsymbol{\Phi}_u,p)-\int_{\Gamma_0}\nabla\boldsymbol{\Phi}_u^T:\mathbf{P}^{-1}$$
$$\cdot\left(\tilde{u}_y\frac{\partial\tilde{\boldsymbol{\tau}}}{\partial\Gamma}+\frac{\partial\tilde{y}}{\partial\Gamma}\tilde{\mathcal{L}}\right)hd\Gamma+\int_{\Gamma_0}\left(\frac{\partial\Phi_u^y}{\partial\Gamma}\mathbf{e}_y\mathbf{e}_y+\frac{\partial\Phi_u^x}{\partial\Gamma}\mathbf{e}_x\mathbf{e}_y\right):\tilde{\boldsymbol{\tau}}hd\Gamma-\int_{\Gamma_0}\frac{\partial\Phi_u^y}{\partial\Gamma}\tilde{p}hd\Gamma$$
$$=0, \tag{A14}$$

$$(\Phi_p,\nabla\cdot\mathbf{u})+\int_{\Gamma_0}\Phi_p\frac{\partial\tilde{u}_y}{\partial\Gamma}hd\Gamma=0, \tag{A15}$$

$$(\boldsymbol{\Phi}_{\dot{\gamma}},\bar{\mathbf{G}}^T-\nabla\mathbf{u})=0, \tag{A16}$$

$$\int_{\Gamma_0}\left(\Phi_h+l^e\frac{\tilde{u}_y}{|\tilde{u}_y|}\frac{\partial\Phi_h}{\partial\Gamma}\right)\left(\frac{h-\hat{h}}{\Theta\Delta t}+\tilde{u}_y\frac{\partial h}{\partial y}+u_y\frac{\partial\tilde{h}}{\partial y}-u_x\right)d\Gamma=0, \tag{A17}$$

with the functionals

$$\mathbf{F}_1[\mathbf{u}(t),\bar{\mathbf{G}}(t^{n+\Theta})]=\mathbf{u}\cdot\nabla\tilde{\boldsymbol{\tau}}-\bar{\mathbf{G}}\cdot\tilde{\boldsymbol{\tau}}-\tilde{\boldsymbol{\tau}}\cdot\bar{\mathbf{G}}^T-G(\bar{\mathbf{G}}+\bar{\mathbf{G}}^T), \tag{A18}$$

$$\mathbf{F}_2[\boldsymbol{\tau}(t)]=\tilde{\mathbf{u}}\cdot\nabla\boldsymbol{\tau}-\tilde{\bar{\mathbf{G}}}\cdot\boldsymbol{\tau}-\boldsymbol{\tau}\cdot\tilde{\bar{\mathbf{G}}}^T, \tag{A19}$$

and

$$\mathbf{P}=\frac{1}{\Theta\Delta t}\mathbf{I}+\left.\frac{\partial\mathbf{F}_3(\boldsymbol{\tau})}{\partial\boldsymbol{\tau}}\right|_{\boldsymbol{\tau}=\tilde{\boldsymbol{\tau}}}, \tag{A20}$$

where $\mathbf{F}_3(\boldsymbol{\tau})$ denotes the function between brackets in Eq. (6) while the Jacobian of this functional $(\partial\mathbf{F}_3/\partial\boldsymbol{\tau}|_{\tilde{\boldsymbol{\tau}}})$ is evaluated around the base flow. The Lagrangian residual of the stationary constitutive relation is defined as

$$\tilde{\mathcal{L}}=-(\tilde{\bar{\mathbf{G}}}\cdot\tilde{\boldsymbol{\tau}}+\tilde{\boldsymbol{\tau}}\cdot\tilde{\bar{\mathbf{G}}}^T)+\mathbf{F}_3(\tilde{\boldsymbol{\tau}})-G(\tilde{\bar{\mathbf{G}}}+\tilde{\bar{\mathbf{G}}}^T). \tag{A21}$$

The additional integrals in Eqs. (A14) and (A15) on the steady state free surface (Γ_0) result from the surface deformations of these free surfaces whereas the new surface shape is determined from the kinematic Eq. (A17). For this equation, special weighting functions have been applied in order to produce nonoscillatory results. Upwinding is performed with the weighting functions

$$\Phi_h+\Delta y\frac{\tilde{u}_y}{|\tilde{u}_y|}\frac{\partial\Phi_h}{\partial y}\approx\Phi_h+l^e\frac{\tilde{u}_y}{|\tilde{u}_y|}\frac{\partial\Phi_h}{\partial\Gamma}, \tag{A22}$$

where Δy is some characteristic length in the y direction of the free surface. Here, we have used the actual length l^e of an element on the surface and the derivatives in the direction of the steady state free surface since $\Delta y\approx n_x l^e$ and $\partial/\partial y\approx(1/n_x)\partial/\partial\Gamma$.

Using the earlier approach, the kinematics of the flow at $t=t^{n+\Theta}$ are obtained from Eq. (A14) to (A17). An update for the polymeric stress is now readily available using these kinematics:

Problem Θ-FEM_step 1^b: Given the base flow $(\tilde{\mathbf{u}},\tilde{\boldsymbol{\tau}},\tilde{\bar{\mathbf{G}}})$ on Ω_0, $\hat{\boldsymbol{\tau}}=\boldsymbol{\tau}(t^n)$, $\mathbf{u}=\mathbf{u}(t^{n+\Theta})$, $\mathbf{G}=\bar{\mathbf{G}}(t^{n+\Theta})$ and $h=h(t^{n+\Theta})$ find $\boldsymbol{\tau}\in\mathcal{T}^h$ at $t=t^{n+\Theta}$ such that for all admissible test functions $\boldsymbol{\Phi}_{\boldsymbol{\tau}}\in\mathcal{T}^h$:

$$\left[\Phi_{\boldsymbol{\tau}}+\frac{h^e}{|\tilde{\mathbf{u}}|}\tilde{\mathbf{u}}\cdot\nabla\boldsymbol{\Phi}\frac{\boldsymbol{\tau}-\hat{\boldsymbol{\tau}}}{\tau_\Theta\Delta t}+\mathbf{F}_1(\mathbf{u},\mathbf{G})+\mathbf{F}_2(\hat{\boldsymbol{\tau}})+\left.\frac{\partial\mathbf{F}_3}{\partial\boldsymbol{\tau}}\right|_{\tilde{\boldsymbol{\tau}}}\cdot\boldsymbol{\tau}\right]$$
$$+\int_{\Gamma_0}\left(\Phi_{\boldsymbol{\tau}}+\frac{h^e}{|\tilde{\mathbf{u}}|}\tilde{\mathbf{u}}\cdot\nabla\boldsymbol{\Phi}_{\boldsymbol{\tau}}\right):\left(\tilde{u}_y\frac{\partial\tilde{\boldsymbol{\tau}}}{\partial\Gamma}+\frac{\partial\tilde{y}}{\partial\Gamma}\tilde{\mathcal{L}}\right)h\,d\Gamma$$
$$=0. \tag{A23}$$

The second step of the Θ scheme [Eq. (A12)] involves the transport problem of the polymeric stress:

Problem Θ-FEM step 2: Given the base flow $(\tilde{\mathbf{u}},\tilde{\boldsymbol{\tau}},\tilde{\bar{\mathbf{G}}})$ on Ω_0, $\hat{\boldsymbol{\tau}}=\boldsymbol{\tau}(t^{n+\Theta})$, $\hat{\mathbf{u}}=\mathbf{u}(t^{n+\Theta})$, $\bar{\mathbf{G}}=\bar{\mathbf{G}}(t^{n+\Theta})$ and $\hat{h}=h(t^{n+\Theta})$, find $\boldsymbol{\tau}\in\mathcal{T}^h$ and $h\in\mathcal{H}^l$ at $t=t^{n+1-\Theta}$ such that for all admissible test functions $\boldsymbol{\Phi}_{\boldsymbol{\tau}}\in\mathcal{T}^h$ and $\Phi_h\in\mathcal{H}^l$:

$$\left[\boldsymbol{\Phi}_{\boldsymbol{\tau}}+\frac{h^e}{|\tilde{\mathbf{u}}|}\tilde{\mathbf{u}}\cdot\nabla\boldsymbol{\Phi}_T\frac{\boldsymbol{\tau}-\hat{\boldsymbol{\tau}}}{(1-2\Theta)\Delta t}+\mathbf{F}_1(\hat{\mathbf{u}},\hat{\bar{\mathbf{G}}})+\mathbf{F}_2(\boldsymbol{\tau})+\left.\frac{\partial\mathbf{F}_3}{\partial\boldsymbol{\tau}}\right|_{\tilde{\boldsymbol{\tau}}}\cdot\hat{\boldsymbol{\tau}}\right]$$
$$+\int_{\Gamma_0}\left(\boldsymbol{\Phi}_{\boldsymbol{\tau}}+\frac{h^e}{|\tilde{\mathbf{u}}|}\tilde{\mathbf{u}}\cdot\nabla\boldsymbol{\Phi}_{\boldsymbol{\tau}}\right):\left(\tilde{u}_y\frac{\partial\tilde{\boldsymbol{\tau}}}{\partial\Gamma}+\frac{\partial\tilde{y}}{\partial\Gamma}\tilde{\mathcal{L}}\right)\hat{h}\,d\Gamma$$
$$=0, \tag{A24}$$

$$\int_{\Gamma_0}\left(\Phi_h+l^e\frac{\tilde{u}_y}{|\tilde{u}_y|}\frac{\partial\Phi_h}{\partial\Gamma}\right)\left[\frac{h-\hat{h}}{(1-2\Theta)\Delta t}+\tilde{u}_y\frac{\partial\hat{h}}{\partial y}+\hat{u}_y\frac{\partial\tilde{h}}{\partial y}-\hat{u}_x\right]d\Gamma=0. \tag{A25}$$

The third fractional step [Eq. (A13)] corresponds to symmetrization of the Θ scheme and is similar to step 1.

A choice remains to be made for the approximation spaces $\mathcal{U}^h$, $\mathcal{T}^h$, $\mathcal{P}^h$, $\mathcal{G}^h$, and $\mathcal{H}^l$. As is known from solving Stokes flow problems, velocity and pressure interpolations cannot be chosen independently and need to satisfy the Babuška–Brezzi condition. Likewise, interpolation of velocity and extra stress has to satisfy a similar compatibility condition. We report calculations using low order finite elements using similar spatial discretizations as were defined by Brown *et al.* (1993) and Szady *et al.* (1995) (continuous bilinear interpolation for viscoelastic stress, pressure, and **G**, and continuous biquadratic interpolation for velocity). We have used linear interpolation functions for the free surface deformation h. Except for the fact that this choice for the approximation space produces nonoscillatory results for the fountain flow problem, there is not yet a mathematical framework available that supports this choice.

C. Boundary conditions

The volumetric flow rate Q is enforced using a Lagrangian multiplier method. If at first we consider a periodic channel flow (for instance the flow depicted in Fig. 1 without the downstream fountain flow) with periodicity for all variables except pressure p. Using the Lagrange multiplier method we need to solve the additional equation on the periodic boundary (Fig. 4):

$$\int_{\Gamma_p^2}\mathbf{u}\cdot\mathbf{n}\,d\Gamma-Q=0, \tag{A26}$$

which determines the flow rate. As a consequence there is a symmetric addition to the momentum equation

$$\Lambda \int_{\Gamma_p^2} \mathbf{\Phi}_u \cdot \mathbf{n} d\Gamma, \tag{A27}$$

where Λ denotes the Lagrange multiplier and $\mathbf{n}$ is the outward normal. If the boundary terms in the weak form of the momentum equations are omitted, it is easily verified that Λ equals the pressure drop over the periodic channel. The boundary contribution can be written as

$$\oint \mathbf{\Phi}_u , \boldsymbol{\sigma} \cdot \mathbf{n} d\Gamma = \int_{\Gamma_p^1 + \Gamma_p^2} \mathbf{\Phi}_u , \boldsymbol{\tau} \cdot \mathbf{n} - p\mathbf{n} d\Gamma = (p_1 - p_2) \int_{\Gamma_p^2} \mathbf{\Phi}_u \cdot \mathbf{n} d\Gamma, \tag{A28}$$

since $\mathbf{\Phi}_u = \mathbf{0}$ on Γ_w, $\mathbf{n}_p^1 = -\mathbf{n}_p^{2-}$ and $\boldsymbol{\tau}(\Gamma_p^1) \cdot \mathbf{n}_p^1 + \boldsymbol{\tau}(\Gamma_p^2) \cdot \mathbf{n}_p^{2-} = 0$. Hence, the constant pressure drop $p_1 - p_2$ is represented by the Lagrange multiplier. For the internal periodic boundary of the fountain flow, this procedure is somewhat more complicated since the sum of the boundary terms now equals

$$\oint \mathbf{\Phi}_u , \boldsymbol{\sigma} \cdot \mathbf{n} d\Gamma = \int_{\Gamma_p^1 + \Gamma_f} \mathbf{\Phi}_u , \boldsymbol{\sigma} \cdot \mathbf{n} d\Gamma. \tag{A29}$$

Clearly Γ_p^1 and Γ_f are not periodic and the earlier analysis fails. However, we may write the right-hand side of Eq. (A29) as

$$\int_{\Gamma_p^1} \mathbf{\Phi}_u , \boldsymbol{\sigma} \cdot \mathbf{n}_p^1 d\Gamma + \int_{\Gamma_p^2} \mathbf{\Phi}_u , \boldsymbol{\sigma} \cdot \mathbf{n}_p^{2-} d\Gamma + \int_{\Gamma_p^2} \mathbf{\Phi}_u , \boldsymbol{\sigma} \cdot \mathbf{n}_p^{2+} d\Gamma + \int_{\Gamma_f} \mathbf{\Phi}_u , \boldsymbol{\sigma} \cdot \mathbf{n}_f d\Gamma. \tag{A30}$$

Since Γ_p^2 is periodic with Γ_p^1 the sum of the first two terms of Eq. (A30) is similar to Eq. (A28). The last term vanishes since we weakly enforce the stress balance ($\boldsymbol{\sigma} \cdot \mathbf{n} = \mathbf{0}$) on the free surface. This leaves only the additional term

$$\int_{\Gamma_p^2} \mathbf{\Phi}_u , (\boldsymbol{\tau} - p\mathbf{I}) \cdot \mathbf{n}_p^{2+} d\Gamma, \tag{A31}$$

which should be included in the governing equations together with Eqs. (A26) and (A27). We will enforce the volumetric flow rate by prescribing the velocity of the reference frame at the mold walls and simply assume $Q = 0$ for both the steady state and stability calculations.

References

Blackwell, R. J., T. C. B. McLeish, and O. G. Harlen, ''Molecular drag-strain coupling in branched polymer melts,'' J. Rheol. **44**, 121–136 (2000).

Bochev, P. B., and M. D. Gunzburger, ''Finite element methods of least-squares type,'' SIAM Rev. **40**, 789–837 (1998).

Bogaerds, A. C. B., A. M. Grillet, G. W. M. Peters, and F. P. T. Baaijens, ''Stability analysis of polymer shear flows using the eXtended Pom–Pom constitutive equations,'' J. Non-Newtonian Fluid Mech. **108**, 187–208 (2002).

Bogaerds, A. C. B., M. A. Hulsen, G. W. M. Peters, and F. P. T. Baaijens, ''Time dependent finite element analysis of the linear stability of viscoelastic flows with interfaces,'' J. Non-Newtonian Fluid Mech. **116**, 33–54 (2003).

Brooks, A. N., and T. J. R. Hughes, ''Streamline upwind/Petrov Galerkin formulations for convection dominated flows with particular emphasis on the incompressible Navier–Stokes equations,'' Comput. Methods Appl. Mech. Eng. **32**, 199–259 (1982).

Brown, R. A., M. J. Szady, P. J. Northey, and R. C. Armstrong, ''On the numerical stability of mixed finite-element methods for viscoelastic flows governed by differential constitutive equations,'' Theor. Comput. Fluid Dyn. **5**, 77–106 (1993).

Bulters, M., and A. Schepens, ''The origin of the surface defect 'slip-stick' on injection moulded products,'' in *Proceedings of the 16th Annual Meeting of the Polymer Processing Society*, Shanghai, China, 2000. Paper IL 3-2, pp. 144–145.

Carvalho, M. S., and L. E. Scriven, ''Three-dimensional stability analysis of free surface flows: Application to forward deformable roll coating,'' J. Comput. Phys. **151**, 534–562 (1999).

Chang, M. C. O., ''On the study of surface defects in the injection molding of rubber-modified thermoplastics,'' in *ANTEC '94*, 1994, pp. 360–367.

Clemeur, N., R. P. G. Rutgers, and B. Debbaut, ''On the evaluation of some differential formulations for the pom–pom constitutive model,'' Rheol. Acta **42**, 217–231 (2003).

Glowinski, R., ''Finite element methods for the numerical simulation of incompressible viscous flow: Introduction to the control of the Navier–Stokes equations,'' in *Vortex Dynamics and Vortex Mechanics*, of *Lectures in Applied Mathematics*, Vol. 28, edited by C. R. Anderson and C. Greengard (American Mathematical Society, Providence, 1991), pp. 219–301.

Glowinski, R., and O. Pironneau, ''Finite element methods for Navier–Stokes equations,'' Annu. Rev. Fluid Mech. **24**, 167–204 (1992).

Graham, R. S., T. C. B. McLeish, and O. G. Harlen, ''Using the Pom–Pom equations to analyze polymer melts in exponential shear,'' J. Rheol. **45**, 275–290 (2001).

Grillet, A. M., A. C. B. Bogaerds, G. W. M. Peters, and F. P. T. Baaijens, ''Stability analysis of constitutive equations for polymer melts in viscometric flows,'' J. Non-Newtonian Fluid Mech. **103**, 221–250 (2002a).

Grillet, A. M., A. C. B. Bogaerds, G. W. M. Peters, M. Bulters, and F. P. T. Baaijens, ''Numerical analysis of flow mark surface defects in injection molding flow,'' J. Rheol. **46**, 651–670 (2002b).

Grillet, A. M., B. Yang, B. Khomami, and E. S. G. Shaqfeh, ''Modeling of viscoelastic lid driven cavity flow using finite element simulations,'' J. Non-Newtonian Fluid Mech. **88**, 99–131 (1999).

Guénette, R., and M. Fortin, ''A new mixed finite element method for computing viscoelastic flows,'' J. Non-Newtonian Fluid Mech. **60**, 27–52 (1995).

Hamada, H., and H. Tsunasawa, ''Correlation between flow mark and internal structure of thin PC/ABS blend injection moldings,'' J. Appl. Polym. Sci. **60**, 353–362 (1996).

Hinch, E. J., ''The flow of an Oldroyd fluid around a sharp corner,'' J. Non-Newtonian Fluid Mech. **50**, 161–171 (1993).

Hobbs, S. Y., ''The development of flow instabilities during the injection molding of multicomponent resins,'' Polym. Eng. Sci. **32**, 1489–1494 (1996).

Inkson, N. J., T. C. B. McLeish, O. G. Harlen, and D. J. Groves, ''Predicting low density polyethylene melt rheology in elongational and shear flows with 'Pom–Pom' constitutive equations,'' J. Rheol. **43**, 873–896 (1999).

Keiller, R. A., ''Numerical instability of time-dependent flows,'' J. Non-Newtonian Fluid Mech. **43**, 229–246 (1992).

Mathieu, L., L. Stockmann, J. M. Haudin, B. Monasse, M. Vincent, J. M. Barthez, J. Y. Charmeau, V. Durand, J. P. Gazonnet, and D. C. Roux, ''Flow marks in injection molding of PP; Influence of processing conditions and formation in fountain flow,'' Int. Polym. Process. **16**, 401–411 (2001).

Mavridis, H., A. N. Hrymak, and J. Vlachopoulos, ''Finite element simulation of fountain flow in injection molding,'' Polym. Eng. Sci. **26**, 449–454 (1986).

Mavridis, H., A. N. Hrymak, and J. Vlachopoulos, ''The effect of fountain flow on molecular orientation in injection molding,'' J. Rheol. **32**, 639–663 (1988).

McLeish, T. C. B., and R. G. Larson, ''Molecular constitutive equations for a class of branched polymers: The Pom–Pom polymer,'' J. Rheol. **42**, 81–110 (1998).

Pearson, J. R. A., *Mechanics of Polymer Processing* (Elsevier Science, New York, 1985).

Sato, T., and S. M. Richardson, ''Numerical simulation of the fountain flow problem for viscoelastic liquids,'' Polym. Eng. Sci. **35**, 805–812 (1995).

Shen, S.-F., ''Grapplings with the simulation of non-Newtonian flows in polymer processing,'' Int. J. Numer. Methods Eng. **34**, 701–723 (1992).

Smith, M. D., R. C. Armstrong, R. A. Brown, and R. Sureshkumar, ''Finite element analysis of stability of two-dimensional viscoelastic flows to three-dimensional perturbations,'' J. Non-Newtonian Fluid Mech. **93**, 203–244 (2000).

Sureshkumar, R., M. D. Smith, R. C. Armstrong, and R. A. Brown, ''Linear stability and dynamics of viscoelastic flows using time-dependent numerical simulations,'' J. Non-Newtonian Fluid Mech. **82**, 57–104 (1999).

Swartjes, F. H. M., ''Stress induced crystallization in elongational flow,'' Ph.D. thesis, Eindhoven University of Technology, November 2001.

Szady, M. J., T. R. Salomon, A. W. Liu, D. E. Bornside, R. C. Armstrong, and R. A. Brown, ''A new mixed finite element method for viscoelastic flows governed by differential constitutive equations,'' J. Non-Newtonian Fluid Mech. **59**, 215–243 (1995).

Verbeeten, W. M. H., G. W. M. Peters, and F. P. T. Baaijens, ''Differential constitutive equations for polymer melts: The Extended Pom–Pom model,'' J. Rheol. **45**, 823–844 (2001).